Astronomy & Astrophysics

Simultaneous visible-near IR photometric study of Kuiper Belt Object surfaces with the ESO/Very Large Telescopes⋆

A. Delsanti[1], O. Hainaut[2], E. Jourdeuil[3], K. J. Meech[4], H. Boehnhardt[5], and L. Barrera[6]

[1] Observatoire de Paris-Medon – LESIA, 5 Place Jules Janssen, 92195 Meudon cedex, France
   e-mail: Audrey.Delsanti@obspm.fr
[2] ESO/Chile – European Southern Observatory, Casilla 19001, Santiago 19, Chili
   e-mail: ohainaut@eso.org
[3] Centre de Recherche Astronomique de Lyon, 9, Av. Charles André, 69561 St-Genis Laval, France
   e-mail: emilie@obs.univ-lyon1.fr
[4] Institute for Astronomy, 2680 Woodlawn Drive, 96822 Honolulu, Hawaii, USA
   e-mail: meech@ifa.hawaii.edu
[5] Max-Planck-Institut für Astronomie, Königstuhl 17, 69117 Heidelberg, Germany
   e-mail: hboehnha@mpia-hd.mpg.de
[6] Universidad Catolica del Norte, Avenida Angamos 0610, Casilla 1280, Antofagasta, Chile
   e-mail: lbarrera@ucn.cl

Abstract. We present simultaneous visible-near-IR *(BVRIJHK)* photometry of 8 Kuiper belt objects (KBOs) and 4 Centaurs. The observations were carried out using two 8m-units of the ESO/Very Large Telescope operated simultaneously on November 29 and 30, 2000. The KBOs displayed linear reflectivity spectra in the optical with a wide range of slopes from neutral (solar) to very red. In most cases, the reflectivity spectra are linear from B to J bands. We notice a change of regime in the spectra which flatten toward the H and K bandpasses. (33128) 1998 BU_{48} even has a significantly negative $H - K$ value. Only (54598) 2000 QC_{243} does not flatten in the infra-red. (24835) 1995 SM_{55} has a noticeably blue spectrum in the near-IR which might be indicative of water ice absorption features. We also present an empirical model for KBO surface evolution, based on models from Luu & Jewitt (1996) and Stern (1995), in which surface colors evolve because of collisions. In the model presented here we propose that cometary activity can refresh the surface. This model predicts that (1) small (e.g. ≪80 km in radius) KBOs should have color variations with rotation, (2) the larger objects should display uniform colors, (3) there should be no color dependence with inclination for objects >100 km in radius, and (4) very distant KBOs are fully irradiated.

Key words. Kuiper belt – minor planets, asteroids – techniques: photometric

1. Introduction

About 700 minor bodies are known to exist in the trans-neptunian region of the Solar System. They are believed to be the brightest, last remnants of the outermost part of the protoplanetary nebula, also known as the Edgeworth-Kuiper belt. In this paper, we call them Kuiper belt objects (KBOs). Dynamically, KBOs are currently distributed in several groups. The Classical belt objects (or *Cubewanos*) have orbits with low eccentricities and inclinations. The resonant objects are trapped in mean motion resonances with Neptune; the largest of these is Pluto, a member of the *Plutinos* sub-group which is trapped in a 3:2 orbital resonance. Finally, the Scattered Disk Objects (SDOs) are on very eccentric orbits, and were ejected into these orbits by interactions with Neptune. KBOs can migrate to the inner Solar System (where they become known as *Centaurs*) either by chaotic "percolation", or after a collision in the belt (which injects either the whole object or fragments, Farinella & Davis 1996). If they escape by collisions with the planets, they can eventually evolve into Short Period Comets (SPCs) if they approach the Sun close enough for a coma to develop.

KBOs formed in the outer region of the solar nebula, which suggests a mixed composition of dust and volatiles. However, because of extrinsic (e.g. collision) and intrinsic (e.g. heating by radioactive decay) processes (Prialnik 2000), the internal structures of these objects have probably been altered.

For instance, it is expected that the largest bodies have, at some point in their history, been completely melted; they are therefore believed to have a fully differentiated structure. In the Kuiper belt, bodies larger than 50–100 km probably retain their primordial size distribution, but bodies smaller than ~20 km diameter are likely to be collisional fragments (Farinella & Davis 1996; Weidenschilling 1997). Unfortunately, theoretical hypotheses are still a long way from being fully confirmed by direct observations. KBOs are faint, the brightest members of the population lie between visual magnitude 20 to 25. This makes physical observations challenging. Only a few spectra are available; some suggest the presence of ices (see Barucci et al. 2004, for a short summary).

The only high signal-to-noise observations that are available for a large sample of objects are multi-color photometric measurements. These types of observations provide only a first insight into the physical properties of KBOs. Various groups have published the results of extensive photometric surveys at visible wavelengths; near-infrared measurements are also available for a more modest sample. Our group has published a compilation of these measurements as well as various statistical tests (Hainaut & Delsanti 2002). We also maintain an up-to-date web-based database of colors (http://www.sc.eso.org/~ohainaut/MBOSS/). In this paper we will refer to the color database as MBOSS, the Minor Bodies of the Outer Solar System. From broadband measurements, it appears that KBOs cover a broad range of colors from neutral to very red, with spectral reflectivity fairly linear over the wavelengths spanned by the B through I filters. Various finer characteristics have been extracted from these data, some of them well established. For instance, cometary nuclei are significantly bluer than the other KBOs (Hainaut & Delsanti 2002; Jewitt 2002). Secondly, a negative correlation between the color of the classical KBOs and their "orbital energy" (defined as $\sqrt{e^2 + \sin^2 i}$) has been found, a correlation that vanishes for the Plutinos. The existence of a "red cluster" of classical KBOs with perihelion distances $q > 40$ AU has been reported by Tegler & Romanishin (2000) and subsequently confirmed (Boehnhardt et al. 2002; Doressoundiram et al. 2003). Other results are still controversial or of poor statistical significance, such as the color-inclination relation for classical KBOs, or the proposed optical color bi-modality (blue-red) of all classes of KBOs (Tegler & Romanishin 1998; Tegler & Romanishin 2000). Peixinho et al. (2003) recently showed that the bimodality confirmed in the sample of KBO colors presented by Tegler & Romanishin (2003) is actually dominated by the Centaur colors; the color bimodality statistically vanishes when Centaurs are removed from Tegler and Romanishin sample. There are some evidence for Centaur color bimodality in the sample of 20 objects measured by Peixinho et al. (2003) (significance level of 99.5% from the dip test on $B - R$ colors). The physical origin of such a color bimodality is not yet understood.

It is interesting to combine the visible and near-IR colors, because this permits us to construct a complete (relative) reflectivity spectrum from 0.4 to 2.2 μm, that could provide clues about surface compositions (e.g. possible ice or organics, natural complex hydrocarbons, absorption features). This provides a first look at the real spectral shape, which is difficult to obtain, even for the brightest objects (because of the high 8 m-telescope cost given the faintness of KBOs). Unfortunately, it is very difficult to obtain simultaneous visible and infrared data. As a consequence, the combination of non-simultaneous data implies some assumptions (which may introduce systematic errors outside of the likely photometric errors). These errors include:

– Changing geometric aspect: this is likely to happen only on timescales of weeks because of the large heliocentric distances and very slow orbital motion of the objects. If the phase angle changes significantly, it is possible to apply an approximate correction to the magnitudes using the IAU H, G formalism (Bowell et al. 1989; McBride et al. 2003) or a simple linear correction (see Sect. 5.1). However, phase effects, in particular at opposition, are poorly documented for KBOs, and this strongly limits the ability to make this correction.

– Brightness changes from rotational light curve modulation: most of the objects are fairly large, thus we can expect them to be fairly spherical. However, there are notable exceptions, such as 20 000 Varuna which has a light curve amplitude of $\Delta m_R = 0.4$ mag (Jewitt & Sheppard 2002) in spite of being one of the largest KBOs. Sheppard & Jewitt (2004) indicate that 15% of the objects he observed show a lightcurve amplitude >0.2 mag. McBride et al. (2003) also suggest that light curve fluctuations of >0.2 mag from rotational modulation or other non-periodic variations are quite common among relatively large objects. Because of $J - K$ band sensitivity limits for detection, it is precisely this group of large objects that we preferentially observe. As a consequence, non-simultaneous data can lead to completely meaningless colors, if care is not taken in the interpretation. Even during quasi-simultaneous visible-near IR observations, light curve effects can require V-band monitoring *during* the J band integration (McBride et al. 2003).

– Transient phenomena: collisions are expected to happen on KBOs, fortunately with a very low frequency. However, transient phenomena do occur; the best documented event being the dramatic change of light-curve morphology of 1996 TO$_{66}$ between 1997 and 1998, which was interpreted as a possible cometary outburst (Hainaut et al. 2000). Another object, (24835) 1995 SM$_{55}$ is suspected to have a non-reproducible lightcurve – which would also be compatible with low-level cometary activity (Sheppard & Jewitt 2004). In addition, there are now several Centaurs that appear to exhibit significant activity: (5145) Chiron (Meech & Belton 1989), C/NEAT (2001 T4) Bauer et al. (2003), and possibly C/2000 B4 and C/2001 M10 (IAU Circ. Nos. 7368 and 7654).

The only way to completely avoid these problems is to simultaneously observe the visible and near-IR colors. We took advantage of the unique facilities offered by ESO's Very Large Telescope, using two of the telescopes on the same nights. We partly put in practice the humorous recommendation that had been made at the MBOSS-1998 workshop, i.e. to use each

of the 4 telescopes with a different filter (Green & McBride 2000). The visible observations and data reduction have been presented in Delsanti et al. (2001). The infrared observations and analysis are described in this paper.

Various processes are suspected to take place to explain the observed KBO color diversity. In particular, a model by Luu & Jewitt (1996), revisited more recently (Jewitt & Luu 2001), involved a reddening of the surface by high-energy particle bombardment, and a surface rejuvenation by impact with smaller KBOs. While this model did a good job of matching the observed color distribution, it had several shortcomings. We have proposed an additional surface rejuvenating process, i.e. recovering the surface with fresh dust lifted by sublimating ice. This model is described and discussed in Sect. 6.

2. Observations

We present Near-IR observations carried out at the ESO Very Large Telescope (VLT), Cerro Paranal, Chile on November 28 and 29, 2000. We used ISAAC (Infrared Spectrometer And Array Camera), installed at the Nasmyth B focus on the Unit Telescope 1 (UT1), in the short wavelength (SW) imaging mode. The SW arm is equipped with a 1024×1024 Hawaii Rockwell array, with a 18.5 μm pixel size projected to 0.148 ″/pixel on the sky. The field of view (FOV) is $2.5' \times 2.5'$. We used the broadband J, H and K_S filters, with central wavelengths of 1.25, 1.65 and 2.16 μm, respectively, and $\Delta\lambda$ of ~0.3 μm.

The telescope was tracked at differential rates, to account for the apparent velocity of the KBOs. Depending on the object's brightness, exposure times from 5 to 50 min were split into individual exposures of typically 1 min duration (themselves split in ~10 s acquisitions) dithered in a random pattern on sky (within 20″ of the central position). The observations were acquired in a sequence of $JHKJ$, the J filter being repeated (for most of the objects) to check for variability. The epoch and conditions of the observations are listed for each object in Table 1.

We also used the FORS2 (FOcal Reducer Spectrograph 2), installed at the Cassegrain focus of UT2, for simultaneous visible ($BVRI$) imaging. Great care was taken to synchronize both telescopes on the same object in order to remove any possible effect of variability. The visible observations and their data reductions are described in detail in Delsanti et al. (2001).

3. Data reduction

The ISAAC data reduction and measurement methods employed here are much more careful than the ones of the standard processing provided by the on-line VLT pipeline or standard software packages. Because the accuracy and reliability of the resulting magnitudes depends greatly on the method used, we shall detail our procedures below.

Electrical ghosts and basic data reduction: we first corrected all the raw data for the "electrical ghosts" with the dedicated Eclipse (Devillard 1997) recipe – "ghost". The electrical ghost in this HAWAII detector is an additional signal proportional
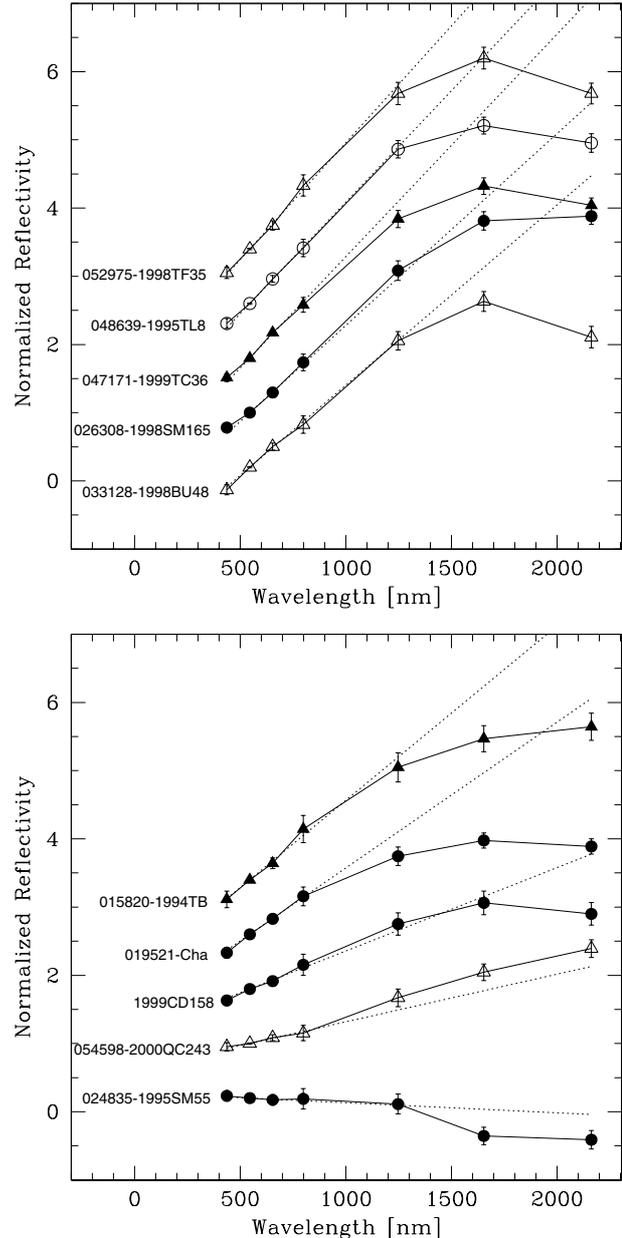
Fig. 1. Normalized reflectivity spectra. Symbols: resonant objects (filled triangles), classical objects (filled circles), centaurs (open triangle), scattered disk objects (open circle). The reflectivities are obtained from the simultaneous $BVRIJHK$ photometry using Eq. (3). The spectra are normalized to 1 at the V filter wavelength and shifted for clarity. The dotted line is a linear fit to the V, R and I reflectivities.

(~10^{-5}) to the total signal intensity which contaminates rows 512 pixels away. A master dark frame (an average of several dark frames with the same exposure time as the science frames) is then subtracted from the raw images. As the ISAAC bias level is a function of the total field illumination, and this correction is not perfect, the residual bias correction will be performed during the sky subtraction phase. Master flat-field frames are generated using the Eclipse recipe "flat", which computes characteristic curves per pixel from a series of twilight exposures. The dark-subtracted images are divided by this master flat-field.

Table 1. Observed magnitudes and observation circumstances.

	Object	Class[1]	UT[2]	r[3]	Δ[3]	α[3]	$J \pm \sigma$	$H \pm \sigma$	$K \pm \sigma$
	1999 CD$_{158}$	Classical	2000/11/30 07:16	48.31	47.72	0.94	20.36 ± 0.07	19.88 ± 0.08	19.90 ± 0.06
			2000/11/30 08:12				20.30 ± 0.07	–	–
	2000 OK$_{67}$	Classical	2000/11/30 00:11	40.83	40.97	1.37	20.55 ± 0.07	20.09 ± 0.05	20.05 ± 0.06
(15820)	1994 TB	3:2	2000/11/30 02:57	29.54	29.08	1.71	20.66 ± 0.08	20.21 ± 0.08	20.09 ± 0.09
(19521)	Chaos†	Classical	2000/11/30 05:49	42.31	41.34	0.21	19.28 ± 0.05	18.86 ± 0.04	18.84 ± 0.04
			2000/11/30 06:45				19.25 ± 0.05	–	–
(24835)	1995 SM$_{55}$	Classical	2000/11/29 03:35	39.39	38.61	0.89	19.56 ± 0.05	19.98 ± 0.05	20.17 ± 0.06
			2000/11/29 03:56				19.48 ± 0.05	20.03 ± 0.05	20.02 ± 0.06
(26308)	1998 SM$_{165}$	2:1	2000/11/29 02:30	34.74	34.16	1.32	19.57 ± 0.07	19.05 ± 0.05	18.97 ± 0.05
			2000/11/29 03:26				19.53 ± 0.07	–	–
(31824)	Elatus†	Centaur	2000/11/29 04:23	8.00	7.04	1.57	–	17.12 ± 0.05	17.10 ± 0.07
(33128)	1998 BU$_{48}$	Centaur	2000/11/29 07:55	27.50	27.22	1.98	19.78 ± 0.05	19.29 ± 0.08	19.41 ± 0.07
			2000/11/29 08:51				19.77 ± 0.05	–	–
(47171)	1999 TC$_{36}$	3:2	2000/11/30 02:14	31.51	31.19	1.70	18.20 ± 0.06	17.75 ± 0.05	17.78 ± 0.04
(48639)	1995 TL$_8$	SDO	2000/11/30 04:25	42.44	41.47	0.83	19.11 ± 0.04	18.71 ± 0.06	18.70 ± 0.06
(52975)	Cyllarus†	Centaur	2000/11/29 05:04	19.24	18.27	0.54	19.49 ± 0.07	19.05 ± 0.06	19.15 ± 0.06
			2000/11/29 06:01				19.51 ± 0.06	–	–
(54598)	2000 QC$_{243}$	Centaur	2000/11/29 00:29	19.40	19.47	2.89	19.57 ± 0.06	19.06 ± 0.05	18.83 ± 0.07

[1]Type of objects, resonances types are from Chiang et al. (2003).
[2]UT start of the sequence.
[3]Helio- and geocentric distances at the time of the observation in [AU], and α is the phase angle in [deg].
† Cyllarus, Elatus and Chaos had respectively the designation 1998 TF$_{35}$, 1999 UG$_5$ and 1998 WH$_{24}$.

Table 2. Optical and Near-IR colors.

	Object	$m_{1,1,\alpha} \pm \sigma$	$m_{1,1,0}^†$	$B - V \pm \sigma$	$V - R \pm \sigma$	$R - I \pm \sigma$	$V - J \pm \sigma$	$J - H \pm \sigma$	$H - K \pm \sigma$
	1999 CD$_{158}$	4.90 ± 0.07	4.78	0.87 ± 0.08	0.48 ± 0.06	0.54 ± 0.09	1.86 ± 0.07	0.45 ± 0.10	-0.02 ± 0.10
	2000 OK$_{67}$	6.13 ± 0.06	5.94	0.73 ± 0.11	0.52 ± 0.07	–	2.42 ± 0.08	0.46 ± 0.08	0.04 ± 0.07
(15820)	1994 TB	7.59 ± 0.09	7.35	1.04 ± 0.12	0.60 ± 0.08	0.70 ± 0.12	2.19 ± 0.09	0.45 ± 0.11	0.12 ± 0.12
(19521)	Chaos§	4.43 ± 0.06	4.40	1.01 ± 0.08	0.58 ± 0.05	0.59 ± 0.08	1.96 ± 0.05	0.40 ± 0.05	0.02 ± 0.05
(24835)	1995 SM$_{55}$	4.32 ± 0.06	4.19	0.63 ± 0.06	0.33 ± 0.06	0.35 ± 0.09	1.00 ± 0.05	-0.42 ± 0.07	-0.19 ± 0.07
		–		–	–	–	1.08 ± 0.05	-0.54 ± 0.07	0.01 ± 0.07
(26308)	1998 SM$_{165}$	5.91 ± 0.05	5.72	0.94 ± 0.07	0.64 ± 0.05	0.652 ± 0.07	2.36 ± 0.07	0.52 ± 0.08	0.08 ± 0.07
(31824)	Elatus§	10.09 ± 0.04	9.95	0.97 ± 0.05	0.65 ± 0.04	0.60 ± 0.07	–	–	0.02 ± 0.08
(33128)	1998 BU$_{48}$	7.03 ± 0.06	6.85	1.10 ± 0.07	0.65 ± 0.05	0.57 ± 0.08	2.27 ± 0.05	0.49 ± 0.09	-0.12 ± 0.10
(47171)	1999 TC$_{36}$	4.88 ± 0.05	4.64	1.03 ± 0.06	0.70 ± 0.04	0.61 ± 0.07	2.34 ± 0.06	0.45 ± 0.07	-0.03 ± 0.06
(48639)	1995 TL$_8$	4.58 ± 0.06	4.46	1.04 ± 0.07	0.69 ± 0.05	0.64 ± 0.08	2.42 ± 0.05	0.40 ± 0.07	-0.02 ± 0.08
(52975)	Cyllarus§	8.51 ± 0.07	8.46	1.13 ± 0.08	0.68 ± 0.07	0.72 ± 0.09	2.42 ± 0.07	0.45 ± 0.09	-0.10 ± 0.08
(54598)	2000 QC$_{243}$	7.95 ± 0.04	7.69	0.72 ± 0.06	0.45 ± 0.04	0.40 ± 0.07	1.69 ± 0.06	0.51 ± 0.07	0.23 ± 0.08

†Errors on $m_{1,1,0}$ are arbitrarily estimated to ~2% more than the σ quoted for $m_{1,1,\alpha}$. This value has been chosen on the basis of measurements from Table 1 in Belskaya et al. (2004); the quoted $m_{1,1,0}$ magnitude takes into account phase effects with some limitations, cf. Sect. 5.1.
‡Index computed from the $J = 19.57 \pm 0.07$, i.e. the closest in time.
§ Cyllarus, Elatus and Chaos had respectively the designation 1998 TF$_{35}$, 1999 UG$_5$ and 1998 WH$_{24}$.

Sky background subtraction: we determined a mask for stars from the set of input images, using the *IRAF/xdimsum* package. For each frame, a sky image is computed by averaging the sky background (masked from the stars) of the preceding and following frames, and is then subtracted out. The number of neighboring frames used to compute the running sky is controlled by the user, and we used a maximum of 10 (to avoid having the sky variations frozen in the computation). The star mask is required to obtain the sky-subtraction accuracy needed for our photometric study. The final result is a set of sky-subtracted images which are automatically combined into a single frame using pixel offsets (obtained from the frame header or determined interactively). However, as explained below, we do not use this automatically combined frame.

Image recombination: because KBOs move with respect to the field stars, the method of image stacking is an important issue. We combined the individual sky-subtracted images in two ways. (i) The individual frames were co-added using multiple star centroids. This composite with point-like stars is used to estimate the Point Spread Function (PSF). However, this image

is not suitable for KBO photometry since objects, moving between two single frames, would appear trailed. (ii) We produce a second composite, taking into account the KBO velocity (obtained from the Horizon ephemeris generator at JPL) to blindly shift the frames using the instrument's known plate scale. In this composite, the object appears point-like while the stars are trailed.

Horizontal line removal and illumination correction: some horizontal lines may remain on the two recombined frames (this is especially obvious in the over-scan of the frames). These structures are an effect of residual bias. They are easily removed by a line by line median filter with rejection using a procedure by Lidman (Priv. Comm.). In addition, some illumination pattern may be present in the frames, which is the result of low-frequency differences between the true flat and the twilight flat. These variations have an rms of 2%. The standard procedure to correct this effect is to image a standard star on a grid of several positions (17 in the case of ISAAC). The next step is to compute the sky corrected standard star fluxes through a fixed aperture, and to fit a two-dimensional, 2nd or 3rd order polynomial to the standard star flux values as a function of position on the array. The illumination correction can be applied to either the data or the flat-field itself. In our case, because the science objects always lie within a few pixels from the center of the chip (i.e. where the illumination effect is the lowest) we judged it sufficient to compute a correction from the 5 position grid of the photometric standard stars imaging template (cf. Sect. 4.1).

4. Photometry

4.1. Standard star reduction and calibration

We used standard stars from the LCO/Palomar NICMOS Catalog (Persson et al. 1998). The standard stars are observed through a dedicated template that images the star at five different positions on the chip. As the telescope offset is relatively large ($\sim$80''), it is possible to obtain the best sky-subtraction by simply subtracting from one image any of the four other images of the sequence. The standard star flux is then measured for each of the five positions with a large aperture (i.e. 15'' diameter) and averaged. We applied the illumination correction directly to the standard star flux (cf. Sect. 3) before computing the telescope zero point. We used Paranal typical extinction values from the ESO calibration plan (which are $k_J = 0.11$, $k_H = 0.06$, and $k_K = 0.07$ mag/airmass). The instrument color transformation was neglected. Solar System objects known $J - K$ colors are below 0.5, and infrared instrument color terms are 1–2%, which makes the contribution of errors from the color transformation well below 1%.

4.2. KBO flux measurement

Due to their faintness, accurate KBO photometric measurements require great care. At near-IR wavelengths, the noise contribution from the sky background can severely contaminate the KBO flux measurements, especially while using large apertures. Our flux calibration procedure differs significantly from the one used for Delsanti et al. (2001). For these reasons, and because it has been suggested that photometric methods may influence the accuracy of the results and therefore the relevance of color distribution structures (Tegler & Romanishin 2000, 2003), we detail the different steps that lead to the final magnitude of the object and an estimate of its error.

Aperture correction photometry: we measure the object flux with an aperture diameter running from 2 to 50 pixels (i.e. 0.3 to 7.5'') using the object's centroid. We next derive a growth profile by plotting total flux versus aperture size. When the flux reaches a plateau, all of the flux from the object is measured. In the near-IR, the signal-to-noise ratio of the images is low. Poor sky estimation while measuring fluxes with a large aperture leads to growth profiles with a poorly defined plateau. It is therefore impossible to perform classical aperture photometry without a significant contamination from the sky background noise. Hence, we use an aperture correction method: the object is measured with a small aperture and we correct the missing flux using a reference curve of growth (obtained from an average of several non-saturated nearby star profiles). This method must be used extremely carefully as (i) the choice of stars for the averaged profile may be problematic in the IR (few non-saturated stars, many barely resolved galaxies, PSF variation over the position on detector) and (ii) this method introduces systematic errors (mainly dominated by the dispersion of the different star profiles) that may not be negligible if not applied carefully. For these reasons, our general strategy is:

1. Construction of a growth profile of the object from the KBO-centered frame. If this profile displays an obvious plateau, it provides a first flux estimate.
2. Selection of stars in the same area of the detector as the science object, but on the star-centered composite: slightly elongated objects are rejected, only the profiles showing a well defined growth curve are kept for *FWHM* estimation and construction of an averaged profile. For each frame, at least 10–15 stars are examined. Sometimes, only 2–3 are kept in the final profile.
3. Aperture correction: the science object is systematically measured with several small apertures ranging from 0.5 to 2 arcsec *FWHM*. For each of these values, the aperture correction is performed utilizing the averaged star growth curve. In this way, we can monitor the stability of the final corrected magnitude as well as the different error contributions for each of the apertures.
4. We compare this aperture-corrected value with the one obtained from the growth profile, if available, and check if it is consistent with the total flux of the object. This last step allows us to identify possible problems with the data and/or the measurements.

4.3. Error estimation

We identify 3 main sources of error: (i) error from the absolute photometric calibration (systematic), (ii) error on the flux measurement, and (iii) error from the aperture correction.

The absolute flux calibration error contribution comes from estimates of the zero-points: standard deviation of the mean value of the 5 images of one given standard star, and error propagation of the flux measurement. The former, which is a consequence of the imprecision of the illumination correction, dominates the latter. The error on the flux measurements includes the standard deviation of the sky photon noise, the photon noise of the object and the detector readout noise (taking into account that we are dealing with recombined frames and sub-frames). Finally, the error on the aperture correction is dominated by the dispersion of the star profiles used to compute the averaged reference profile. All of the error contributions are summed quadratically to obtain an estimation of the final error on the magnitude, and for this run the errors are typically 6%, which is compatible with the ISAAC performance in the range of S/N we are dealing with. The final magnitudes and their total 1σ uncertainties are listed in Table 1.

5. Results

5.1. Magnitudes and colors

We present data for the observing circumstances and the derived magnitudes in Table 1. Infra-red colors are listed in Table 2. We also report the visible colors that were observed simultaneously with the IR data and published in Delsanti et al. (2001). The quantity, $m(1, 1, \alpha)$, is the absolute magnitude defined as:

$$m(1, 1, \alpha) = R - 5 \log (r\Delta), \tag{1}$$

where R is the magnitude through filter R at the time of the observations (i.e. at a helio- and geocentric distances r and Δ [AU], and phase angle α [deg]). To take account of the phase effects, we used an empirical linear correction:

$$m(1, 1, 0) = R - 5 \log (r\Delta) - \beta\alpha. \tag{2}$$

The current measured values are $\beta = 0.09$ for Centaurs (Bauer et al. 2003) and $\beta = 0.14$ for the other objects (which is the mode of the values published in Sheppard & Jewitt 2002). However, these values (which are very different from the $\beta = 0.04$ obtained for a couple of comets) should be taken with great care. Indeed, for KBOs, phase functions can only be determined for very small phase angles. These steep slopes might be due to measurements done close to the opposition surge (non linear regime of the phase curve). For these reasons, the $m(1, 1, 0)$ values in Table 2 are presented only for information.

We converted the magnitudes $m(\lambda)$ into relative spectral reflectivities $\mathcal{R}(\lambda)$, computed at the central wavelength of our broadband filters used, using the formula from Jewitt & Meech (1986):

$$\mathcal{R}(\lambda) = 10^{-0.4[m(\lambda)-m(\lambda)_\odot]}. \tag{3}$$

We normalized the reflectivities computed from Eq. (3) to the central wavelength of the V filter. Because the visible and near-IR data were obtained simultaneously, we were able to construct a visible-near IR low resolution reflectivity spectrum for each object, shown in Fig. 1 without any assumptions regarding the variability of the objects.

5.2. Discussion

Spectral reflectivities and colors: Fig. 1 shows that objects display a rather linear reflectivity spectrum over the visible wavelengths with a change of regime that seems to occur beyond 1 μm. The range of visible slopes of our sample runs continuously from neutral (24835 1995 SM$_{55}$ with a VRI spectral gradient of -1.14 ± 3.58 %/100 nm, cf. Delsanti et al. 2001) to very red (52975 Cyllarus with 36.67 ± 3.79%/100 nm, same ref.).

For most of the objects, the J band reflectivity is, within the error bars, consistent with the visible spectrum. A direct, practical consequence is that simultaneous V and J observations (at perhaps high telescope cost and difficult observational logistics) are not necessary, since the information might be inferred from the visible photometry alone. If observers are investing telescope time in the IR, it is worthwhile to perform a complete JHK sequence (if object brightnesses permit it) rather than measuring a single J magnitude.

For 19521 Chaos, and to a lesser extent (54598) 2000 QC$_{243}$ and (41171) 1999 TC$_{36}$, the linearity of the spectra over the $V - J$ range is not as obvious. 1999 TC$_{36}$ is a binary KBO: the objects have a 0.4″ separation and a difference of magnitude of 2.2 (Trujillo & Brown 2002). The two components are not resolved on our frames where the KBO image is fairly circular. We therefore cannot determine which component and configuration we observe. However we assume that, due to the brightness difference of the components, we measure the flux from the brightest object. Any eclipsing effect (for instance the extreme case of the smallest object in front of the biggest one) should not affect the observed J magnitudes and more generally the colors in a significant way, even if the objects are different. The overall shape of the spectrum of (41171) 1999 TC$_{36}$ is consistent with the spectro-photometric results obtained by Dotto et al. (2003) in September 2001 with VLT+ISAAC. From a combination of the visible spectrum from Lazzarin et al. (2003) and their IR spectrum, Dotto et al. suggest a tentative model of surface composition with a mixture of *tholin* (a mixture of nitrogen and methane), amorphous carbon and water ice.

(54598) 2000 QC$_{243}$ has an intriguing red slope in the infrared and the J reflectivity does not follow the linear trend of the optical spectral gradient. This is a little bit puzzling considering that the optical and infrared sequences were executed during *exactly* the same timespan, and that there is no obvious problem with the data or the photometry and no potential contamination from a nearby object. Unfortunately, the infrared spectrum obtained by Dotto et al. (2003) is not complete (the J band is missing). However, our JHK colors are systematically redder than theirs (our $J - H$ is 0.16 mag higher and our $H - K$ is only marginally compatible). Their values seem closer to what one should expect from KBO infrared colors. Dotto et al. find a $\Delta J = 0.5$ variation over 3 days, therefore sampling different phases of the 0.7 mag amplitude lightcurve presented by Ortiz et al. (2002). Light curve effects and the overall shape of the spectrum of (54598) 2000 QC$_{243}$ deserve further study.

We notice a general change of regime in the spectral reflectivities which flattens toward the K magnitude. Some of the objects even have a negative $H - K$ color. (33128) 1998 BU$_{48}$ has a $H - K = -0.12 \pm 0.10$, which is compatible with independent measurements with the same instrumental setup from observations taken in April 2001 for the ESO large Program (paper in preparation). In these observations, $H - K$ is even more significantly negative. Sheppard & Jewitt (2002) obtained a lightcurve for this object and derived a peak-to-peak variation of 0.68 ± 0.04 mag over 4.9 h. Negative values of $H - K$ might hint at the presence of a broad absorption band. At these wavelengths (i.e. greater than 1.65 μm), organics (for instance *Titan tholins*, although they should be regarded as artificial end-members of models, cf. Moroz et al. 2003) or crystalline water ice (see below) might play this role. Such objects therefore deserve a complete spectroscopic study.

(24835) 1995 SM$_{55}$ has a noticeably blue spectrum. Crystalline water ice has a broad, deep absorption centered near 2.05 μm, roughly 0.3 μm wide. In the H ($\lambda_{\text{cent}} = 1.65$ μm) and K ($\lambda_{\text{cent}} = 2.16$ μm) filters (both $\sim$ 0.3 μm wide), a strong water ice absorption will reduce the flux and cause a negative broad band reflectivity spectrum. More generally, blue colors may indicate the presence of fresh ices which are susceptible to sublimation. An interpretation of the non-repeatable lightcurve observed by Sheppard & Jewitt (2004) is that the object might undergo cometary activity. (24835) 1995 SM$_{55}$ is therefore a good candidate for dust coma search as was performed for (24952) 1997 QJ$_4$ (Meech et al. 2004). The infrared color variations 1995 SM$_{55}$ displayed during our run are within the photometric errors bars and are therefore not significant. McBride et al. (2003) measured the object twice, separated one month apart. The variation of the J magnitude (corrected for distance) ranged from 0.11–0.18 (comparing with our two J mags) to 0.14–0.25 (after linear correction for phase effects). Another object that we have in common with McBride et al. (2003), (26308) 1998 SM$_{165}$ (a binary KBO discovered by Brown & Trujillo 2002), differed by 0.55 mag in J band. Since both studies were quite careful in their photometric analysis methods, this confirms that lightcurve effects may not be uncommon among even large KBOs (McBride et al. 2003).

Trends: statistical tests on the latest version of the MBOSS colors database (including $\sim$25 objects in the near infrared) does not show any evidence for a significant correlation between infrared colors and orbital parameters a, e, i, q nor absolute magnitude $M_{(1,1,\alpha)}$. However, this should not be regarded as a definitive result, as the number of objects is still too low for significant statistical conclusions.

Figure 2 plots two optical-infrared color-color diagrams which are a compilation of all simultaneous $V - J$ colors published to date (using the MBOSS database). The thin curve is the locus of objects with linear reflectivity spectra (which we call hereafter the "reddening curve", see Delsanti et al. 2001). It is worth noting that this curve is not a straight line in a color-color plot, as one might intuitively think. The objects follow this curve fairly well which means that the objects have a nearly linear spectrum over the $V - J$ range. This confirms that (i)
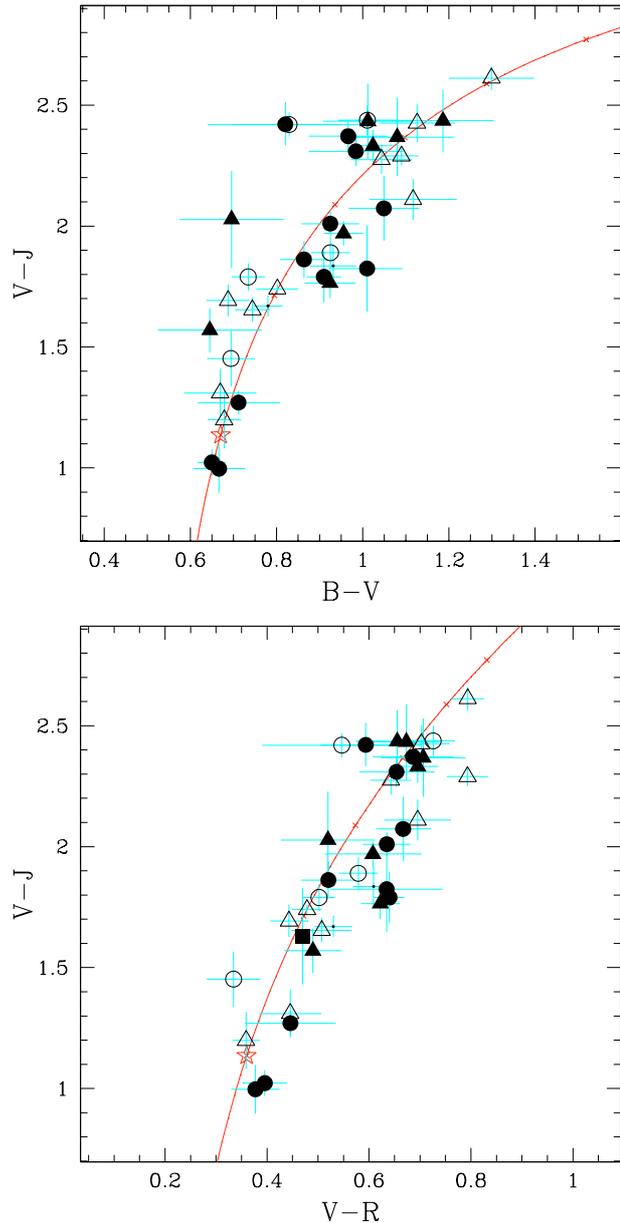
Fig. 2. Color color plots of the averaged colors from the updated version of the compilation presented in Hainaut & Delsanti (2002). The star indicates solar colors. Symbols have the same meaning as in Fig. 1. The thin curve represents the locus of objects with a linear reflectivity spectrum as described in Delsanti et al. (2001). The broad correlation between $B - V$ and $V - J$ mentioned by McBride et al. (2003) is not as obvious in this larger sample. (This figure is available in color in electronic form.)

visible colors alone are sufficient to give insight on the overall spectral shape up to $\sim$1 μm; (ii) spectral shapes in the $V - J$ region are consistent with a single reddening agent (as previously mentioned by Jewitt & Luu 2001; McBride et al. 2003). Using the full database, the broad linear correlation between the visible and $V - J$ mentioned by McBride et al. (2003) can be refined into a match with the reddening curve rather than a linear relation.

We would like to draw the attention of the reader to the fact that a linear correlation between visible and infrared colors does not imply that objects have a linear reflectivity spectrum
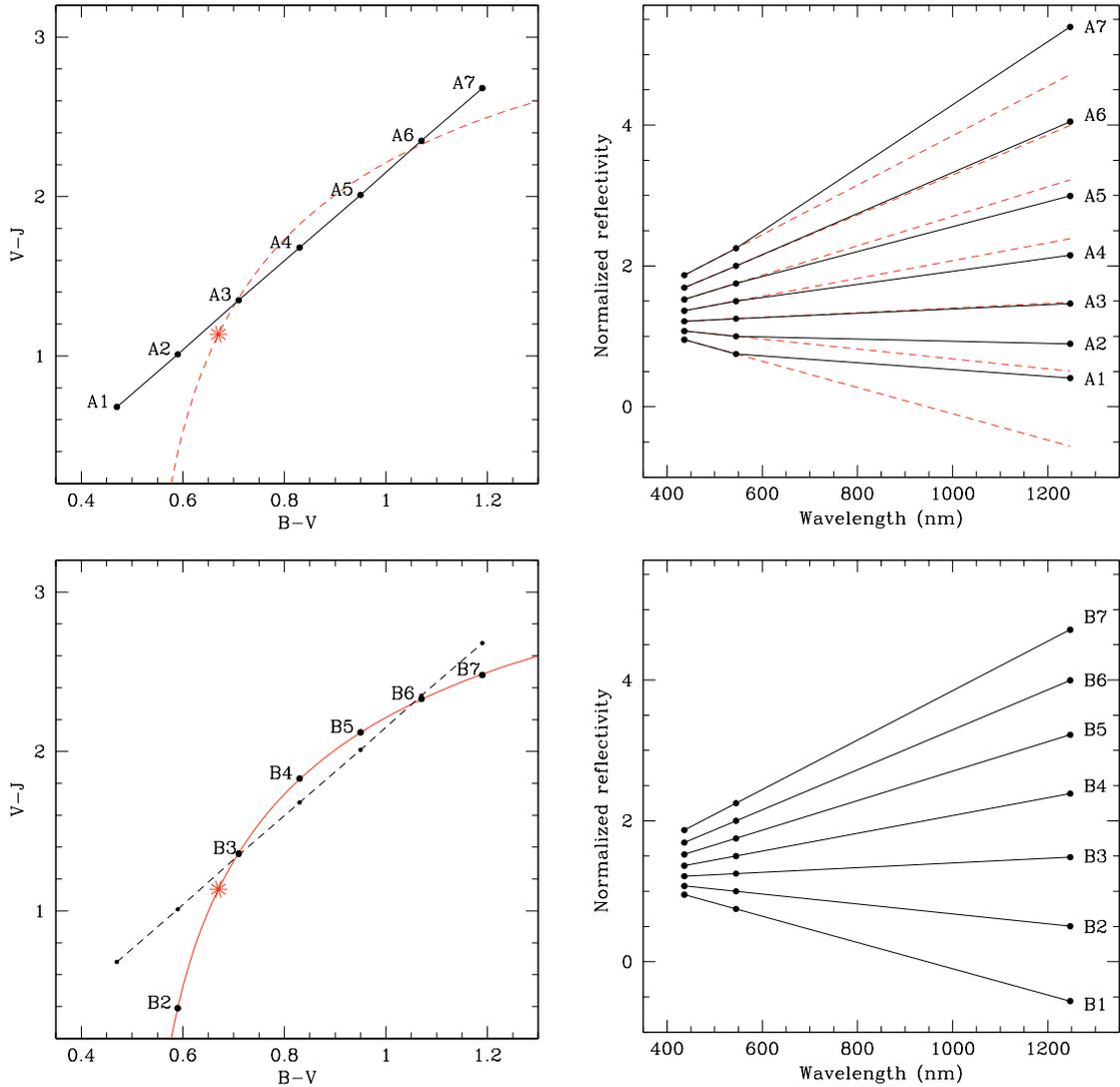
Fig. 3. Left panels are color-color diagrams. The star indicates solar colors. Right panels are the corresponding reflectivity spectra (using Eq. (3), normalized to 1 in the *V* band and shifted for clarity). Linear color correlations (straight line on top left quadrant) might be useful to derive infrared reflectivities from visible observations. However, they do not imply that objects following such a correlation have a *linear* reflectivity spectrum (see spectra of objects A1 to A7, top right panel). Perfectly linear spectra (bottom right, objects labeled B1 to B7) correspond in fact to a curve in a color-color diagram (plain curve in bottom left quadrant and dashed curve in top left quadrant). (This figure is available in color in electronic form.)

over the $V - J$ range, although it may allow to infer *J* reflectivities from visible observations and it is consistent with a single reddening agent. To illustrate this idea, we used the linear correlation in the $B - V$, $V - J$ space computed for instance by McBride et al. (2003) (Fig. 3, straight line in top left quadrant). We picked points on that line with a regular $B - V$ sampling to simulate objects. For these objects, we plotted the corresponding reflectivity spectra, which are displayed in Fig. 3, in the top right quadrant. These spectra are in general *not* linear (this is especially obvious for object A1). Perfectly linear spectra (Fig. 3 bottom right) on the other hand give a color-color plot as displayed in the bottom left quadrant: the objects follow the "reddening curve" (objects B1 to B7). In conclusion, objects that display a linear color correlation do not necessarily have a linear reflectivity spectra. Their general spectral shapes along the correlation line can even be read directly from the color-color plot (top left quadrant): it is concave-up when the object

is "above" (i.e. redder in $V - J$) the reddening curve (objects A1, A2, A7), linear when the correlation line is crossing the reddening line (objects A3, A6), and convex when the object is "below" (i.e. bluer) the reddening curve (objects A4, A5).

In conclusion, KBO reflectivity spectra can be described with a single parameter over the $V \longrightarrow J$ range, suggesting that the reddening is caused by a single agent as opposed to various independent ones. This single parameter is the slope of the spectrum itself.

6. Modeling KBO surface evolution

The present photometric study confirms the broad range of KBO surface colors – from neutral to very red, already observed by several groups (see Doressoundiram 2004, for a review). Physically, several explanations have been proposed. First, KBOs might have intrinsic different compositions.

A model by Gomes (2003) describes how planetesimal migrations during formation can lead to a Kuiper belt composed of minor bodies formed in very different regions of the Solar System.

Another possibility is that the observed color diversity is the result of various surface evolution processes. KBOs are believed to be composed of ices mixed with different compounds (organics and minerals). The surfaces of the objects are supposed to be permanently irradiated by high-energy particles (galactic cosmic rays, solar wind particles) and short wavelength radiation which breaks the hydrogen atom bonds, resulting in a progressive polymerization of the ices. Laboratory experiments studied the effect of ion irradiation (one of the effects of the "space weathering") on ices and organics. Fresh ices initially display a blue spectral continuum in the optical and a high visual albedo. With increasing irradiation doses, ices first become optically red and dark (lower albedo at bluer wavelengths). The formation of an irradiated mantle (dark, hydrogen-poor, carbon-rich) is expected. Indeed, when ices contain carbon, a refractory residue is formed, which after irradiation evolves into a hydrogenated amorphous carbon with neutral colors (Moroz et al. 2004; Strazzula 1998, for a review). After long-term irradiation, ices get a spectral continuum back to neutral with a very low albedo at all wavelengths (Andronico et al. 1987; Thompson et al. 1987). Moroz et al. (2003) recently experimented on natural complex hydrocarbons. They originally have a red spectral continuum in the visible-near infrared range and are optically dark. Irradiation-induced carbonization gradually lead to neutral spectra.

Luu & Jewitt (1996); Jewitt & Luu (2001) have simulated the diversity of colors using a model involving two processes: a reddening, exponential with time, to represent the aging by irradiation, in competition with stochastic non-disruptive collisions with smaller KBOs, to rejuvenate the surface by excavation of fresh (neutral) underlying material. This model is successful at representing the total range and distribution of object colors. However, it predicts color variations with the object's rotation (i.e. within a few hours) and a size dependency of the objects with color that have not been observed to date.

We have revisited this model and added cometary activity as an additional rejuvenating process. Cometary activity is indeed a very efficient resurfacing process, either by excavating and/or re-covering the surface with fresh (non-irradiated) dust lifted by gas outbursts. Water-ice driven activity rapidly decreases between 4–6 AU from the Sun, as illustrated by the production rates as a function of the heliocentric distance in Fig. 4 from Meech & Svoren (2004). However, both amorphous water-ice crystallization and annealing as well as sublimation of more volatile species such as CO_2 and CO can take place at much larger heliocentric distances.

Distant activity is now routinely observed at $r = 10-15$ AU: Chiron's coma was discovered at ~12 AU (Meech & Belton 1989) (even displaying a tail at 9 AU Hainaut 1994), outburst of comet 1P/Halley at 14.5 AU (West et al. 1991), activity of C/1995 O1 (Hale-Bopp) at 17.5 AU. A few cases of activity beyond 20 AU have been reported, for example comet C/1987 H1 (Shoemaker) at 20 AU, Meech et al. (2004). There are even cases of activity suspected in one KBO – from the

change in the light curve of 1996 TO$_{66}$ (Hainaut et al. 2000). Additionally, Pluto's surface is known to display some sublimation phenomena. For a summary of cometary activity, see Meech & Hainaut (2001); Meech et al. (2004).

6.1. Description

6.1.1. Parameters of the model

In this model we will follow the evolution of the $V - R$ color of a test object affected by 3 processes (aging by irradiation, collisions and cometary activity – described below).

The spherical test object is characterized by its radius, R_N [km], and orbital parameters (a, e, i) from which we derive its heliocentric distance, r, at any step of the simulation. The surface is divided into a matrix of 50×100 elements. Each of these elements has the following characteristics: $V - R$ color, a collision flag (indicating whether it has undergone collision during the running time step), a cometary activity flag (indicating whether the surface element under consideration is currently active), and a crust thickness (initialized to 0 m, the crust represents the upper layer of the object, that is fully depleted of all volatiles by irradiation or sublimation).

We can operate this model with a coarse time step (typically 10^{5-6} yr) to investigate the slow trends of the surface, or with a fine time step (~1 month to 1 yr) to monitor fast changes, for instance the onset of cometary activity. It must be noted that this model does not take any dynamical evolution into account: an object will remain on its orbit as long as we run the simulation, even if this is far beyond the dynamical life time of such orbit.

6.1.2. Aging by irradiation

Our current knowledge of KBO surface compositions does not permit us to clearly assume any proportion of fresh ices versus organics. From laboratory experiments, it appears that both materials behave differently under ions irradiation. As mentioned above, blue-sloped spectra of fresh ices become redder and then neutral again, while red-sloped organic spectra gradually neutralize. Nonetheless, both behaviors are not completely incompatible; one can expect that organics might be in part the product of fresh ices aging (which become neutral again after long-term irradiation). For these reasons and uncertainties, we decided to follow the simple formalism of Luu & Jewitt (1996, 2001). They simulated the aging by irradiation of the object by an exponential reddening with time:

$$V - R = (V - R)_\odot \, e^{-t/T_c} + (V - R)_{max}, \qquad (4)$$

where an object initially having a solar, neutral color $(V-R)_\odot = 0.36$ at time $t = 0$, will redden exponentially toward $(V-R)_{max}$, the maximum $V - R$ value observed among real KBOs (set to 0.9 from the MBOSS color database) in a timespan T_c years. In parallel with the reddening of the surface, the upper layer of the object is depleted of volatiles, forming an irradiation crust. Corresponding to the penetration depth of cosmic rays in an icy material (Johnson et al. 1987), typical estimates for crust thickness are around 1 m. We calibrated the formation of a 1 m

crust in $T_c = 10^8$ years (Shul'Man 1972; Luu & Jewitt 1996), as the surface evolves from neutral to fully reddened.

It must be noted that this model does not reproduce the turn back to neutral of surfaces with long term irradiation. The model presented in this paper is meant as a simple empirical test to check for the possibility of cometary activity as a factor for explaining the KBO color distribution. For this reason, in the framework of the model, initial ($t = 0$) colors are set to neutral, and a fully irradiated surface will have a red (i.e. $V - R = 0.9$). In addition, choosing the same formalism as Luu & Jewitt (1996) will help for the analysis and comparison of the results.

6.1.3. Collisions

We used the collision model developed by Stern (1995), which considers non-disruptive collisions between members of the Kuiper belt. Luu & Jewitt (1996) detailed why is it reasonable to consider that a collision of a 1 km-sized body onto a 100 km target (assuming a density of 10^3 kg m^{-3}) will result in cratering rather than complete target disruption. Stern adopted a "particle-in-a-box" formalism where the collision rate depends on "the local space density of impactors, the local average crossing velocity of the target body against the Kuiper belt population at heliocentric distance $r(t)$, and the collision cross section of the impactor+target pair, corrected for gravitational focusing". Stern also computed a table of characteristic collision time-scales as a function of impactor and target sizes. We used these values, scaled to the heliocentric distance of the object using a r^{-2} profile to simulate the density decrease of the Kuiper belt, and to the plane of the ecliptic (using a 10° *FWHM*) to determine if the test KBO undergoes a collision during a particular time step. We set a sharp inner limit to the Kuiper belt at 38 AU. Within that heliocentric distance, we reduce the collision rate by a factor of 10^6, to approximate the more recent model by Durda & Stern (2000) who find that the frequency of collisions in that region is orders of magnitude smaller than farther out in the Kuiper belt. This approach allows us to compute and store in advance the collision timescales needed, therefore reducing considerably the computer execution time.

In the case of a collision, the impact position on the object is chosen at random. The size of the crater and the ejecta blanket are computed using the same formalism as Luu & Jewitt (1996): the crater radius R_{crater} is a function of the impactor radius a_P and of the test-object radius a_T (in m), using the scaling law for cratering in ice by Lange & Ahrens (1987):

$$R_{crater} = 6.7 \times 10^2 \, a_P^{0.69} \, a_T^{0.31}. \qquad (5)$$

The object is recovered by an ejecta blanket of excavated neutral material at the impact position and on a surrounding region of radius $R_{blanket}$ defined as:

$$R_{blanket} = 10 \, R_{crater} \qquad (6)$$

This size was choosen by Luu & Jewitt (1996) as a conservative value of the range (from 10 to 50 times the crater size) quoted by Housen et al. (1983). The crust thickness of the region is also reset to 0m to reflect the fact that excavated material is fresh ice.
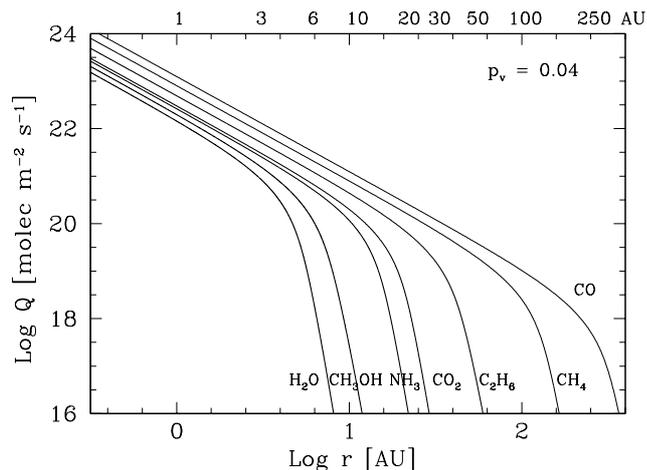

Fig. 4. Sublimation rates of various ices from Meech & Svoren (2004) after Delsemme (1982).

6.1.4. Cometary activity

We construct a very simple model of cometary activity to examine the effect on the color distributions. Prialnik et al. (2004) computed gas production rates for sublimation of pure volatiles for rapidly rotating nucleus of albedo $p_V = 0.04$ (Fig. 4). The production rates decrease very quickly with the distance, but do not reach zero. At large distances, there is some level of gas leaving the nucleus but the flux might not be sufficient to drag dust into an observable coma (Meech & Svoren 2004). To simply model this effect, we decided to set a sharp cut-off of H_2O activity to 5 AU, CO_2 to 14 AU, CO to 120 AU. These values correspond to the heliocentric distances at which the vapor pressure drop with temperature starts to dominate the shape of the production rates (cf. Fig. 4). We set an arbitrary crust thickness for a surface element, under which cometary activity is possible, (i.e. 2 m, 1 m, 0.5 m for the 3 species considered). These thicknesses should represent only the relative depletion of the upper surface of the comet for each of the different volatiles. This simple vision has limitations; in reality, other effects influence the cometary activity. For instance, heat is accumulated in the nucleus at perihelion, permitting sublimation at larger distances on the outbound leg of the orbit compared to the inbound leg. These effects are not considered.

Hence, for a given object, cometary activity of a surface element is triggered when (i) the crust thickness is low enough for the corresponding volatile to sublimate and (ii) the heliocentric distance of the object is such that a volatile can sublimate. This implies that cometary activity can be spontaneous (i.e. thermally-induced, because the crust thickness allows it) or collision-induced (a collision reduces the crust thickness enough to release a burst of volatiles). Once activity is triggered, the object is not necessarily resurfaced by the freshly excavated dust. Indeed, the re-deposition of dust onto the active object depends on its size and its heliocentric distance. The expansion velocity of a dust halo (in m s^{-1}) depends on the heliocentric distance r as (Bobrovnikoff 1954):

$$v_{exp} = \frac{580}{\sqrt{r}} \sqrt{\frac{\mu_0}{\mu}}, \qquad (7)$$
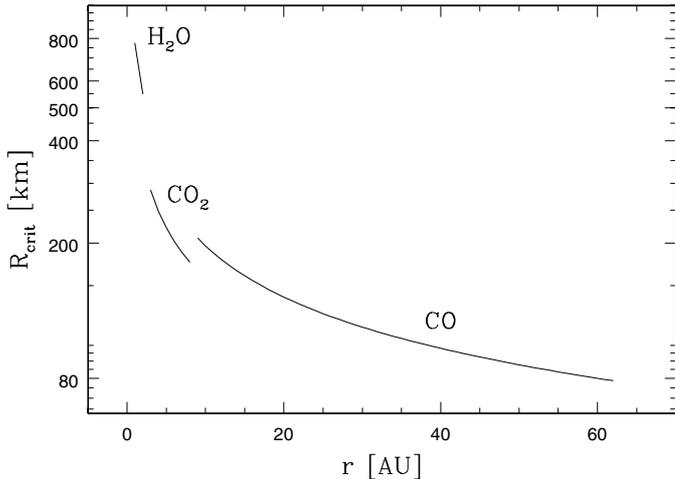
Fig. 5. Variations with the heliocentric distance of the critical radius above which an object is able to keep its bound coma.

where μ is the molecular weight of the volatile with respect to water, μ_0. The ratio, μ_0/μ, is equal to 0.41 for CO_2 and 0.64 for CO. The escape velocity of a particle from a body of radius R_N and mass M is given by:

$$v_0 = \sqrt{\frac{2GM}{R_N}}, \qquad (8)$$

where G is the gravitational constant. If we consider a spherical KBO of density ρ, we can infer a critical radius R_0 above which the dust halo will not be lost, forming a traditional coma. From Eqs. (7) and (8) we derive:

$$R_0 = \frac{580}{\sqrt{r}} \sqrt{\frac{\mu_0}{\mu} \frac{3}{8\pi G\rho}}. \qquad (9)$$

When a burst of cometary activity is triggered, if the radius of the KBO is greater than R_0 (computed assuming $\rho = 10^3$ kg m^{-3}), the object is able to retain a bound coma of fresh, neutral colored dust, which results in the complete resurfacing of the object. Also, when a surface element is sublimating, its crust is thickening. In this way, we represent the depletion of volatile in the upper surface layer (the growth rate is calibrated so that a Halley-type comet is completely suffocated by its crust in a few hundred revolutions). The variation of the critical radius with heliocentric distance is illustrated in Fig. 5. Again, in this simple model, no dust size distribution is considered; either the object is big enough to keep enough dust to refresh the surface, or it is not.

6.2. Tests and results

We simulated test objects with sizes picked discretely in the 1–500 km radius range and explored the e, i space for values corresponding to different dynamical classes. We therefore tested orbital eccentricities ranging from 0 to 0.99 (this last extreme value is to check for the behavior of short period comet-like objects), inclinations from 0 to 12° (i.e. about the thickness *FWHM* of the Kuiper belt), and orbit semi-major axes a from 10 to 80 AU. We also picked real orbital parameters for known
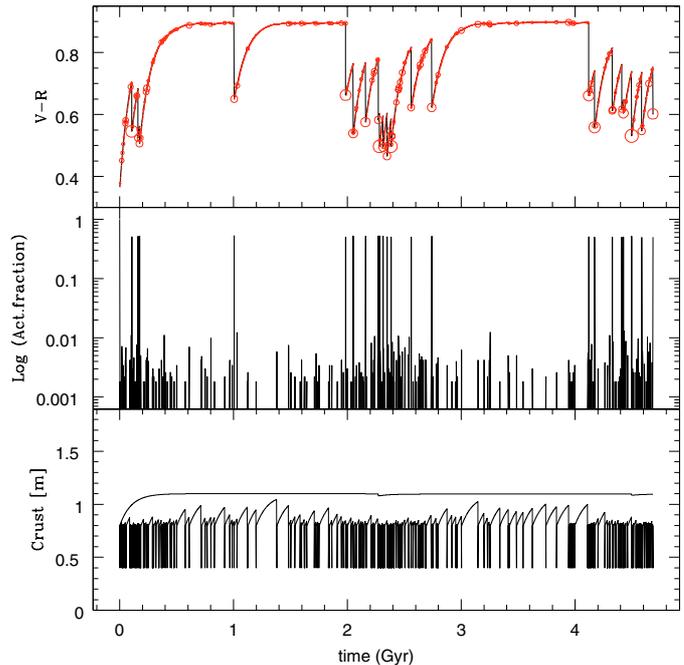
Fig. 6. Evolution of a Plutino on a circular, inclined orbit. The top panel displays the variations of the average color of the object. Collisions are indicated by a circle whose size is logarithmically related to that of the impactor. The second panel shows the fraction of the surface on which ice sublimation occurs, and the third one the minimum and maximum thickness of the crust over the surface of the object. (This figure is available in color in electronic form.)

objects (5145 Pholus, 2060 Chiron, 1996 TL$_{66}$, 1P/Halley and C/1995 O1 (Hale-Bopp)) to validate our results. As a very first test, we ran the model with only two surface evolution processes: reddening by irradiation and rejuvenation by collisions. We were thus able to directly compare our results with those of Luu & Jewitt (1996); Jewitt & Luu (2001). As expected, both works arrived at the same results and conclusions.

Because of CPU time limits (a full model takes up to 1 h to run on a dual-processor Sun Enterprise workstation), we did not perform statistics from Monte-Carlo-like simulations involving large numbers of test objects. Instead, we considered the various time-steps of single objects over the steady states appearing in its evolution. Some simulations were conducted with the fine time step of ~1yr in order to verify that the simple representation of cometary activity from our model produced realistic comets. For instance, the very general behavior of a Halley-type comet is reproduced (of course, within the limitations of the simple model, which is not meant to compete with sophisticated radiation transfer models far beyond the scope of this work). It includes the slow decrease of activity, eventually resulting in the complete cessation of activity after many revolutions, corresponding to the formation of a mantle of material completely depleted of volatiles. All the simulations described in what follows were performed with the coarse time step (e.g. 10^{5-6} year) which permits us to study the test objects over a time scale sufficient for collisions and reddening to play a significant role.

6.2.1. Example

Figure 6 displays the evolution of a *Plutino*-like object on an inclined circular orbit, including the effects of the 3 processes described above. The color evolution shows a general trend from fresh surface to completely irradiated, with occasional resurfacing by an impact (the impact occurrences and size of impactor are marked by circles on the $V - R$ plot). As expected, larger impactors resurface a larger fraction of the object, causing a deeper dip in the color curve. The figure also shows the fraction of the surface that is sublimating and the minimum and maximum thickness of the crust. When the object suffers a collision, the crust is destroyed over a fraction of the surface (depending of the size of the impactor) which might become active. After the next time step (e.g. 10^{5-6} yrs in the coarse sampling mode), in case cometary activity was triggered, that area is depleted of volatiles, the activity stops, and the reddening starts over for that region. In the case of a large KBO, the collision-triggered activity rejuvenates the complete surface (by bound coma redeposition), and the object is reset to a uniform neutral color.

6.2.2. Size effects: Bound coma and color variegations

Within the region where cometary activity is possible (i.e. $r < r_{CO}$ in the model), the simulations show that objects larger than the critical radius for their heliocentric distance display uniform colors, thanks to the complete re-surfacing by ballistic dust. However, objects smaller than this radius show contrasted spots of different colors. This effect is present no matter what the collision rate or the overall object colors.

This model therefore reproduces the fact that the observed objects do not present color variations over their rotation; it also predicts that the smallest objects should present noticeable color variations over their rotation. The data available to date do not permit verification of this prediction, as very few, very small objects have been observed repetitively; a test would be to compare multi-color light curves of objects with very faint absolute magnitudes.

6.2.3. Distance effects

The model predicts four regimes of resurfacing as a function of the heliocentric distance of the minor body. These are:

From 0 AU to r_{H_2O}: the heliocentric distance under which water driven cometary activity is supposed possible, set here to 5 AU. The water sublimation completely dominates the surface evolution, and the effect of collisions is completely negligible. In that region, the critical radius for an object to retain a ballistic coma is much larger than any realistic object (see Fig. 5), so all the dust is lost; the objects are comets. Once a surface element is depleted of volatiles, its color will start to redden, but with a timescale longer than the dynamical lifetime of a comet. For the model, we took a 5 km object that we let evolve for 3 Gy in the Kuiper belt before removing it and putting it on a short-period comet orbit. The surface elements that had a crust

thinner than 1 m (the limit set for H_2O simulation) became active. As this has to be done using the more CPU intensive "short time step", only one such experiment was performed. In that experiment, the comet became bluer than the original KBO ($V - R = 0.4$ instead of 0.6), which is in agreement with the comets being on average bluer than KBOs (Hainaut & Delsanti 2002; Jewitt 2002).

The Centaurs: we simulated the evolution of the surface of 5145 Pholus and 2060 Chiron-like objects of radius from 1 to 100 km, using their real orbital parameters. For both type of orbits, the object's lifetime is dominated by irradiation reddening effects during which they get an increasingly thick crust. As they evolve in the inner part of the Solar System, (i.e. where our model uses very low collision rates (see Sect. 6.1.3), cometary activity is triggered with also a very low probability. The increasing thickness of the crust prevents the objects from developing a spontaneous burst of cometary activity, even at distances where volatiles can sublimate. Cometary activity mainly occurs when a collision happens, which is very unlikely over the dynamical lifetime of a Centaur. Hence, simulations for both object types lead to very red objects regardless of the size. In that framework, an object like 5145 Pholus and 7066 Nessus (both $V - R = 0.79$) represent the typical surface characteristics of an evolved Centaur.

2060 Chiron, which has a neutral $V - R = 0.36 \pm 0.03$ (from an average of 29 epochs of the MBOSS colors database) is active. Its observed color is compatible with the idea that the surface is being resurfaced by the bound coma detected by Meech et al. (1997). However, the model (based on Durda & Stern 2000) indicates that it is unlikely that its activity was triggered by a collision. It has been suggested that some of the SPCs and Centaurs could be fragments of larger objects ejected from the belt by collision (Farinella & Davis 1996). As such a fragmentation would expose fresh, volatile rich interior of the object, this would support the presence of active and/or neutral-blue (10370 Hylonome, 2000 EC$_{98}$, (54598) 2000 QC$_{243}$) Centaurs – Chiron would in that case just be recovering from its ejection. Also, the typical dynamical lifetime of a Centaur (10^6 yr) is fairly short compared to the irradiation time scale. We suggest that their color diversity represents scars acquired while still in the Kuiper belt. In that framework, the color bimodality that Peixinho et al. (2004) have reported and statistically quantified could indicate that the very red objects are old Centaurs that have been fully irradiated, while the neutral ones have been recently injected in the inner solar system, and are either still cometary active, or have just started the reddening process. If true, this hypothesis predicts that we should be able to find other Chiron-like active Centaurs among the neutral-blue ones. Also, it would be interesting to investigate whether the orbits of the blue and/or active centaurs correspond to recent injections, while the very red ones are stable and/or more ancient.

The main Kuiper belt: at heliocentric distances between the inner edge of the Kuiper belt (set to 38 AU in the model, see Sect. 6.1.3) and r_{CO} (the heliocentric distance under which CO driven activity is supposed possible), the three processes
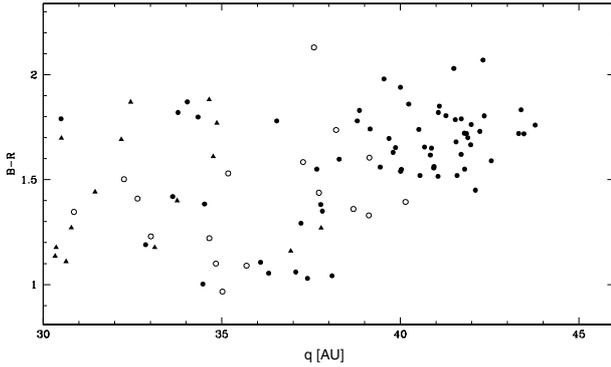
Fig. 7. Color of the KBOs as a function of their perihelion distance q in AU (from Hainaut and Delsanti on-line datase; Classical KBOs are shown as filled circles, SDOs as open circles, and Plutinos as filled triangles). A lack of blue objects with very large q and a red cluster of classical KBOs at $q > 40$ AU is clearly displayed.

are in competition. Cometary activity is driven by CO and either starts spontaneously provided the mantle thickness is low enough to produce a burst or is triggered by a collision. In this regime, when the size of the KBO is big enough to retain a bound coma, cometary activity is very efficient at completely rejuvenating the objects surface. The complete range of colors from solar to very red is reproduced and, as discussed in Sect. 6.2.2, large objects have uniform colors, while small objects are predicted to show color variations over their rotation.

Outer zone of the Kuiper belt, with a heliocentric distance greater than r_{CO}. In this region where collisions are sparse (due to the collision rate decreasing as r^{-2}, r being the heliocentric distance) and where cometary activity is not possible in the frame of the model, the reddening strongly dominates, leading to fully irradiated objects.

Figure 7 displays the color of the KBOs (from the MBOSS database) as a function of their perihelion distance in AU. The lack of blue, distant objects (i.e. bottom right of the plot), which is also suggested by Tegler & Romanishin (2000) (who reported a cluster of red classical objects at $q > 40$), could be the first hint of this effect. The model predicts that, if there are some objects remaining all the time beyond the region where cometary activity is plausible, they will display optical colors corresponding to a long term irradiation state of the surface, regardless of the size. In our simple model, we assumed that the maximum irradiation state leads to optically red colors ($V - R = 0.9$). However, if we consider Thompson et al. (1987); Andronico et al. (1987) experiments on ices and Moroz et al. (2003) on organics, radiation dose increases, representing long term exposure to galactic cosmic rays, gives rise to progressively neutral surfaces with an extremely low albedo at all wavelengths. We are in the process of including this effect in a future version of this model, that will replace the simple reddening function by actual laboratory spectra.

6.2.4. Colors vs. inclination

For "classical KBOs" with extreme radii, the model predicts no influence of the inclination on the color. For very small

objects (with any inclination), the collisions are so infrequent that they are insufficient to significantly rejuvenate the surface (which end up red). For very big objects, the collision rate (combined with the activity driven resurfacing) is large enough (even at high i) to fully compensate the reddening (and the objects remain blue). Finally, for intermediate radii (10–100 km, i.e. large enough to suffer collisions, but not massive enough to retain ejected dust), objects on inclined orbits tend to be redder. Indeed, as the collision rate decreases with inclination, the rejuvenation of the surface decreases too. As the critical radius for classical KBOs is of the order of ~100 km, this could affect only the faintest objects.

The MBOSS color database indicates that color is anti-correlated with the inclination, with a correlation coefficient of -0.6 to -0.8 depending on the color. The same trend is observed with respect to the "collision energy" parameter $\mathcal{E} = \sqrt{e^2 + \sin^2 i}$, with similar correlation coefficient. These trends are statistically strongly significant, with t-tests probabilities to be random effect at the 10^{-3} to 10^{-4} level. Our model considers only the position of the object in the Solar System to assign a collision; its energy is related only to the size of the impactor. The inferred inclination-related prediction for intermediate radii and blue trend for the largest objects are not observed. We therefore conclude that the "collision energy" parameter $\mathcal{E}$ plays an important role in the determination of the collision rates in the Kuiper belt (which is not taken into account in the model we used from Stern 1995).

6.3. Summary

We presented the first simultaneous optical-infrared *BVRIJHK* photometry measurements obtained with two 8m telescopes for 8 KBOs and 4 Centaurs. We reconstructed their relative spectral reflectivities which are fairly linear over the $V \longrightarrow J$ range, and generally flatten toward infrared magnitudes. (24835) 1995 SM$_{55}$ is a significantly blue object – perhaps displaying water-ice features. The odd behavior of the infrared reflectivity spectrum of (54598) 2000 QC$_{243}$ in this study should be checked by other observations. Both J magnitude variations over rotation and/or poor agreement of infrared measurements between several studies may imply (as already mentioned by McBride et al. 2003) that light curve effects might be common among KBOs, even for the largest members that are rather expected to be spherical.

A very simple model was developed to simulate the color diversity of KBOs, involving a reddening by irradiation, a resurfacing by non-disruptive collisions with smaller KBOs, and a cometary sublimation possibly causing a resurfacing by ballistic dust redeposition for large objects. The results of this model are the following:

– The general broad lines of the long term evolution of a comet is reproduced, i.e. it becomes slowly covered by a crust that reduces the total active surface, decreases the total activity and finally turns the object into an inert body.
– The simulated objects reproduce the observed color range and distribution for the KBOs. The resurfacing caused by cometary activity is much more uniform than that caused

by impacts, The objects therefore do not present rotational color effects, as is currently observed among KBOs. These color variations were one of the major flaws of previous models which did not include activity. The model also indicates that very small KBOs (≪80 km) will display color variations over their rotation.

- No color dependence with inclination is produced, except for objects of intermediate size (10–100 km), where it predicts a correlation opposite to that which is observed. We conclude that the effect of average collision energy ($\sqrt{e^2 + \sin^2 i}$, which is not taken into account in the model) dominates the effect of a decreased collision frequency.

- Centaurs remaining long enough on their orbits will become fully irradiated, e.g. like 5145 Pholus. However, as the typical dynamical lifetime of a Centaur is short compared to the irradiation time scale, we suggest that Chiron could have just been ejected to the Centaur region by collision that would have exposed its volatile-rich interior. Similarly, other neutral-blue Centaurs should display cometary activity.

- We also predict that very distant KBOs (i.e. beyond the region where activity can play a significant role) will be fully irradiated, resulting in very dark albedo. This is supported by the observed lack of neutral-blue objects with large perihelion distances, and could contribute to the lack of discovered objects with $q > 45$ AU.

References

Andronico, G., Baratta, G. A., Spinella, F., & Strazzulla, G. 1987, A&A, 184, 333

Barucci, A., Doressoundiram, A., & Cruikshank, D. 2004, Comets II, in press

Bauer, J. M., Fernández, Y. R., & Meech, K. J. 2003, PASP, 115, 981

Belskaya, I., Barucci, A., & Shkuratov, Y. 2004, First Decadal Review of the Edgeworth-Kuiper Belt, in press

Bobrovnikoff, N. T. 1954, ApJ, 59, 356

Boehnhardt, H., Delsanti, A., Barucci, A., et al. 2002, A&A, 395, 297

Bowell, E., Hapke, B., Domingue, D., et al. 1989, Asteroids II, 524

Brown, M. E., & Trujillo, C. A. 2002, IAU Circ., 7807

Chiang, E. I., Jordan, A. B., Millis, R. L., et al. 2003, ApJ, 126, 430

Delsanti, A. C., Boehnhardt, H., Barrera, L., et al. 2001, A&A, 380, 347

Delsemme, A. H. 1982, Comet Discoveries, Statistics, and Observational Selection, IAU Colloq., 61, 85

Devillard, N. 1997, The Messenger, 87, 19

Doressoundiram, A. 2004, First Decadal Review of the Edgeworth-Kuiper Belt, in press

Doressoundiram, A., Tozzi, G. P., Barucci, M. A., et al. 2003, ApJ, 125, 2721

Dotto, E., Barucci, M. A., Boehnhardt, H., et al. 2003, Icarus, 162, 408

Durda, D. D., & Stern, S. A. 2000, Icarus, 145, 220

Farinella, P., & Davis, D. R. 1996, Science, 273, 938

Gomes, R. S. 2003, Icarus, 161, 404

Green, S., & McBride, N. 2000, Minor Bodies in the Outer Solar System, 57

Hainaut, O. 1994, Ph.D. Thesis, Université de Liège and European Southern Observatory

Hainaut, O. R., Delahodde, C. E., Boehnhardt, H., et al. 2000, A&A, 356, 1076

Hainaut, O. R., & Delsanti, A. C. 2002, A&A, 389, 641

Housen, K. R., Schmidt, R. M., & Holsapple, K. A. 1983, J. Geophys. Res., 88, 2485

Jewitt, D., & Meech, K. J. 1986, ApJ, 310, 937

Jewitt, D. C. 2002, AJ, 123, 1039

Jewitt, D. C., & Luu, J. X. 2001, AJ, 122, 2099

Jewitt, D. C., & Sheppard, S. S. 2002, AJ, 123, 2110

Johnson, R. E., Cooper, J. F., Lanzerotti, L. J., & Strazzulla, G. 1987, A&A, 187, 889

Lange, M. A., & Ahrens, T. J. 1987, Icarus, 69, 506

Lazzarin, M., Barucci, M. A., Boehnhardt, H., et al. 2003, ApJ, 125, 1554

Luu, J., & Jewitt, D. 1996, AJ, 112, 2310

McBride, N., Green, S. F., Davies, J. K., et al. 2003, Icarus, 161, 501

Meech, K., Hainaut, O., Boehnhardt, H., & Delsanti, A. 2004, First Decadal Review of the Edgeworth-Kuiper Belt, in press

Meech, K., & Svoren, J. 2004, Comets II, ed. M. Festou, et al. (Tucson, AZ: Univ. AZ. Press), in press

Meech, K. J., & Belton, M. J. S. 1989, IAU Circ., 4770, 1

Meech, K. J., Buie, M. W., Samarasinha, N. H., Mueller, B. E. A., & Belton, M. J. S. 1997, ApJ, 113, 844

Meech, K. J., & Hainaut, O. R. 2001, Tidal and Collisional Interactions of Small Bodies in the Solar System, ed. M. Ya., Marov, & H., Rickman (Dordrecht: Kluwer), 163

Moroz, L., Baratta, G., Distefano, E., et al. 2004, First Decadal Review of the Edgeworth-Kuiper Belt, in press

Moroz, L., Baratta, G., Strazzula, G., et al. 2003, Icarus, submitted

Ortiz, J. L., Baumont, S., Gutiérrez, P. J., & Roos-Serote, M. 2002, A&A, 388, 661

Peixinho, N., Boehnhardt, H., Belskaya, I., et al. 2004, Icarus, submitted

Peixinho, N., Doressoundiram, A., Delsanti, A., et al. 2003, A&A, 410, L29

Persson, S. E., Murphy, D. C., Krzeminski, W., Roth, M., & Rieke, M. J. 1998, ApJ, 116, 2475

Prialnik, D. 2000, Minor Bodies in the Outer Solar System, ed. Fitzsimmons, Jewitt, & West (Springer), 9

Prialnik, D., Benkhoff, J., & Podolak, M. 2004, in Comets II, ed. M. Festou, et al. (Tucson, AZ: Univ. AZ. Press) in press

Sheppard, S., & Jewitt, D. 2004, First Decadal Review of the Edgeworth-Kuiper Belt, Earth Moon and Planets, in press

Sheppard, S. S., & Jewitt, D. C. 2002, ApJ, 124, 1757

Shul'Man, L. M. 1972, The Motion, Evolution of Orbits, and Origin of Comets, IAU Symp., 45, 265

Stern, S. A. 1995, ApJ, 110, 856

Strazzula, G. 1998, Solar System Ices, 281

Tegler, S., & Romanishin, W. 2000, Nature, 407, 979

Tegler, S., & Romanishin, W. 2003, Icarus, 161, 181

Tegler, S. C., & Romanishin, W. 1998, Nature, 392, 49

Thompson, W. R., Murray, B. G. J. P. T., Khare, B. N., & Sagan, C. 1987, J. Geophys. Res., 92, 14933

Trujillo, C. A., & Brown, M. E. 2002, ApJ, 566, L125

Weidenschilling, S. J. 1997, Icarus, 127, 290

West, R. M., Hainaut, O. R., & Smette, A. 1991, A&A, 246, L77